Materials Today Communications 51 (2026) 114741

Contents lists available at ScienceDirect

Materials Today Communications

journal homepage: www.elsevier.com/locate/mtcomm

Assessment of the Fe-Si-B eutectic composition using calorimetry and microstructural analysis

Amirhossein Ghavimi [a,*], Maryam Rahimi Chegeni [a], Lucas Ruschel [a], Bastian Adam [a], Marcos Rodríguez-Sánchez [c,d], Maria Teresa Perez-Prado [c], Isabella Gallino [b], Ralf Busch [a]

[a] Saarland University, Chair of Metallic Materials, Campus C6.3, Saarbrücken 66123, Germany
[b] Technical University of Berlin, Chair of Metallic Materials, Ernst-Reuter-Platz 1, Berlin 10587, Germany
[c] IMDEA Materials Institute, Calle Eric Kandel, 2, Getafe, Madrid 28906, Spain
[d] Science and Engineering Department, Universidad Carlos III de Madrid, Av. De la Universidad 30, Leganés, Madrid 28911, Spain

ARTICLE INFO

Keywords:
Fe-Si-B alloy
Eutectic composition
Thermal analysis
Microstructure
Intermetallic
Glass forming ability

ABSTRACT

Eutectic compositions in potentially glass forming binary or ternary alloy systems are usually the starting point to identify metallic liquids in search of an increased glass-forming ability (GFA). The Fe-Si-B ternary system has great potential if it could be additively manufactured via laser bed powder fusion into large, intricate soft magnetic parts for using in highly energy-efficient devices such as motors. However, the GFA of the currently available alloys is low to print fully amorphous parts, making alloy development necessary. Therefore, this study assesses Fe-rich Fe-Si-B alloys in term of eutectic point, which has not been accurately explored over the past four decades. A combination of differential thermal analysis, phase analysis via X-ray diffraction, and microstructural characterization through optical microscopy and scanning electron microscopy in the relevant composition range reveals that the eutectic composition of the Fe-Si-B system with a high Fe content is found to be at or close to $Fe_{77}Si_{11}B_{12}$ at% with a eutectic temperature of 1388 K (1115 °C). Thermal analyses and microstructural studies reveal a sharp melting peak and a well-defined phase transition into the distinct eutectic lamellae, composed of Fe_2B and α-Fe/Fe_3Si. Deviations from the eutectic composition either at Si-rich or at B-rich side result in the formation of primary simple dendritic (Fe_3Si) or faceted dendritic (Fe_2B) phases, respectively, which precede eutectic solidification. The GFA study using high-energy XRD of the cast plates reveals that the eutectic composition does not necessarily exhibit the maximum critical casting thickness and GFA can be enhanced by strong glass-forming elements in off-eutectic compositions.

1. Introduction

Iron-silicon-boron (Fe-Si-B) alloys are utilized in a wide range of applications, including thermal energy storage systems [1], wear-resistant coatings [1], power transformers, efficient electric motors [2], and high-performance electronic devices [3]. Its most notable application lies in the electrical industry due to its exceptional soft magnetic properties, which are achieved by rapidly quenching Fe-B-Si-based alloys into the amorphous state or by producing a very fine nanocrystalline microstructure (e.g., Finemet [4]) by annealing of the rapidly quenched amorphous alloys. In any case, so far, the critical thickness to form a glassy Fe-Si-B alloy has been limited to below 100 μm. The commercially available ones are industrially produced by melt-spinning ribbons with thicknesses of 50 μm or thinner. The limited glass forming ability (GFA) of Fe-Si-B-based alloys makes it difficult to manufacture larger and intricate parts and restricts industrial applicability. Therefore, the development of alloys that are more robust with respect to crystallization is desirable.

This becomes especially attractive since in the past decade the advancement of additive manufacturing of metals has also led to efforts to additively manufacture (AM) glassy alloys by laser powder bed fusion (LPBF), in which the fast cooling rate during the LPBF or printing of the individual layers is most beneficial to promote glass formation. Indeed, in one of the first partially successful efforts, an Fe-based metallic glass was printed via LPBF [5]. Later, e.g., Zr- [6], Cu- [7], and Ni-based [8] alloys were printed fully glassy using the same technique. However, it turns out that a critical thickness of 100 μm is not sufficient to print a fully glassy part, even though the cooling rate during LPBF is

---

[*] Corresponding author.
E-mail address: Amirhossein.Ghavimi@uni-saarland.de (A. Ghavimi).

https://doi.org/10.1016/j.mtcomm.2026.114741
Received 29 June 2025; Received in revised form 10 January 2026; Accepted 26 January 2026

comparable to the rate achieved during melt spinning, as was shown during printing of commercially available conventional Fe-Si-B-based alloys of the Kuamet-type [9,10] or Finemet-type [11]. Thus, the Fe-Si-B-based alloys require rigorous alloy development to improve GFA by at least one order of magnitude and make them suitable for 3D printing via LPBF.

The earliest criterion for a good GFA dates back to David Turnbull [12]. He defined the so-called reduced glass transition temperature ($t_{rg}= T_g/T_l$), where T_l is the liquidus temperature, and T_g is the glass transition temperature. The larger the t_{rg}, the better the GFA. In good oxide glass formers and very deep eutectics of metallic liquids, t_{rg} approaches 0.6–0.66. The glass transition temperature in an alloy system is relatively constant as a function of composition. Thus, it is generally accepted that high GFA is found in or close to eutectic alloys, where T_l has a minimum and consequently t_{rg} becomes larger.

Over the past three decades, many glass-forming alloys have been developed to form metallic glass with thicknesses exceeding 1 mm, commonly referred to as bulk metallic glasses (BMG). These alloys are multicomponent eutectic alloys, generally including 3–5 components, where the constituent atoms exhibit a significant size mismatch. This results in metallic liquids at judiciously chosen compositions [13] that have a very high packing density with pronounced medium- and short-range order, bringing them thermodynamically closer to the competing crystalline phases, which reduces the driving force for crystallization. The high packing density also leads to that these alloys are highly viscous [14], slowing down the nucleation and growth kinetics [15,16]. All these BMG forming liquids have in common that they were developed by starting with one or more deep binary eutectics to find an even lower eutectic in the multicomponent composition space. To apply this strategy to Fe-Si-B alloys, it is crucial to identify the eutectic point as a starting step in developing Fe-based soft magnetic metallic glasses with higher GFA for 3D printing [17].

The ternary Fe-Si-B alloy system exhibits three eutectic points. According to literature, these are a Fe-rich (e.g., $Fe_{74}Si_8B_{18}$ [18]), a B-rich ($Fe_{42}Si_{10}B_{48}$ [19]), and a Si-rich ($Fe_{40}Si_{31.6}B_{28.4}$ [20]) eutectic. Since the soft magnetic properties are the most interesting feature of the Fe-Si-B system, this study focuses on the Fe-rich eutectic composition since a higher Fe content enhances magnetic properties. The literature review of Fe-rich Fe-Si-B alloys reveals widespread data, indicating eutectic compositions without definitive consensus on a unique ternary eutectic composition. Early studies on the Fe-Si-B system by Smith and Wever in the 1930s laid the foundation for understanding its phase equilibria, using thermal analysis and metallography [21]. Subsequent advancements in experimental techniques, X-ray diffraction (XRD) and electron probe microanalysis, refined the findings [22]. Ames et al. introduced a compositional eutectic range as a patent aimed at amorphous strip production, consisting of 77–79 at% Fe, 5–7 at% Si, and 13–16 at% B with an eutectic temperature of 1422 K (1149 °C) in 1986 [23]. Gibson and Delamore studied the crystallization behavior of the compositions $Fe_{78}Si_9B_{13}$ and $Fe_{78}Si_{10}B_{12}$ in 1990 that the $Fe_{78}Si_{10}B_{12}$ alloy composition approximates a eutectic trough in the Fe-Si-B phase diagram [24]. Yamasaki et al. studied the viscosity of some Fe-Si-B alloys and assumed $Fe_{79.5}Si_{12}B_{8.5}$ as eutectic in 1992 [25]. The development of computational methods, particularly the CALPHAD (Calculation of Phase Diagrams) approach, further advanced the understanding of the Fe-Si-B system, enabling predictions of phase equilibria and enhancing the reproducibility of experimental results [19]. Poletti and Battezzati proposed the $Fe_{74}Si_8B_{18}$ at% composition as the eutectic point, which was computed by CALPHAD at 1334 K (1061 °C) in 2013 [18]. Furthermore, Huang et al. experimentally investigated the nano-eutectic formation of $Fe_{83}Si_1B_{16}$ and $Fe_{83}Si_2B_{15}$ in 2016 [26]. Fan et al. analyzed the recalescence process and interface growth of the apparent eutectic $Fe_{82}Si_1B_{17}$ alloy in 2018 [27]. Yue et al. discussed the magnetic properties of several Fe-Si-B compositions as eutectics and close-eutectics in 2019 [28].

The final objective is to identify Fe-Si-B-based alloy compositions to form BMGs with critical casting thicknesses exceeding 1 mm. Therefore, this study revisits the Fe-rich portion of the Fe-Si-B phase diagram to reassess the solidification and melting behavior to determine the Fe-rich eutectic point. To pinpoint it, a combination of thermal analysis, X-ray diffraction, and microstructural investigations using optical and scanning electron microscopy is applied.

2. Materials and methods

2.1. Sample preparation

Alloy ingots (Fig. 1a) were synthesized from high-purity elements: Fe (99.97 wt%), Si (99.95 wt%), and B (99.5 wt%). The weighted elements were cleaned in an ultrasonic bath using acetone and ethanol and subsequently alloyed according to the specific quantities of the desired composition in an arc-melting furnace on a water-cooled copper hearth under a high-purity Ti-gettered argon atmosphere (99.999 % Ar) to minimize oxidation. The ingots were flipped and remelted five times to obtain homogeneity. The weight losses during preparation and after arc melting were determined to be generally less than 0.2 wt% of the total ingot weight of 16 g. Fig. 1 illustrates the prepared Fe-Si-B samples for characterizations and microstructural studies.

To study GFA, the Fe-Si-B plates with thicknesses of 140 ± 10 μm, 250 ± 10 μm, and 350 ± 10 μm were produced by a suction casting machine. The master alloy was melted in an arc melter on a water-cooled copper hearth and suction-cast into the mold cavity under vacuum, resulting in rapidly quenched plate-shaped samples.

2.2. Calorimetric analysis

The solidus temperature (T_s) and liquid temperature (T_l) of the master alloys were determined using a NETZSCH STA 449 Jupiter differential thermal analyzer. At the eutectic temperature and composition, only the phases of the eutectic microstructure form; the solidus temperature equals to the eutectic temperature ($T_s = T_{eut}$), and no primary phase is present. Small samples with a weight of about 100–120 mg cut from the ingots were heated to 1573 K or 1623 K in Al_2O_3 crucibles (Fig. 1b) to a fully molten state with a heating rate of 2, 4, 20, and 50 K/min (0.033, 0.067, 0.333, 0.833 K/s, respectively). The molten metal was subsequently solidified with a cooling rate of 4 K/min (0.067 K/s) to obtain a coarse microstructure that is close to equilibrium. This results in spherical samples with an average diameter of 2.5–3 mm (Fig. 1c). Lower cooling rates were initially explored to approach equilibrium conditions further; however, a rate of 2 K/min led to oxidation in several alloy samples. This behavior is attributed to the high oxidation susceptibility of Fe-rich Fe-Si-B alloys (Fe > 70 at%), combined with the prolonged residence time in the molten state and possible interactions with the crucible at elevated temperatures. Consequently, a cooling rate of 4 K/min was selected as a practical compromise, ensuring oxidation-free solidification while maintaining sufficiently slow cooling to allow reliable assessment of near-equilibrium eutectic microstructures.

All DTA experiments were performed in multiple repetitions, depending on the alloy composition and the analysis purpose. Measurements of key alloy compositions (alloys #4, #10, and #16) exceeded four times, the microstructurally investigated ones at least three times, and all remaining alloys at least twice. Thermal values are reported as mean values with an experimental uncertainty of ±3 K, especially in Table 1, accounting for both measurement variability and the limitations of the tangent method.

2.3. X-ray diffraction

X-ray diffraction was used to study the structure of the solidified phases using Cu Kα-radiation ($\lambda = 0.15406$ nm) within an angular range of $20^\circ < 2\theta < 80^\circ$ and a resolution of 0.02°. The required flat sample surface for the XRD experiment was obtained by grinding the lateral

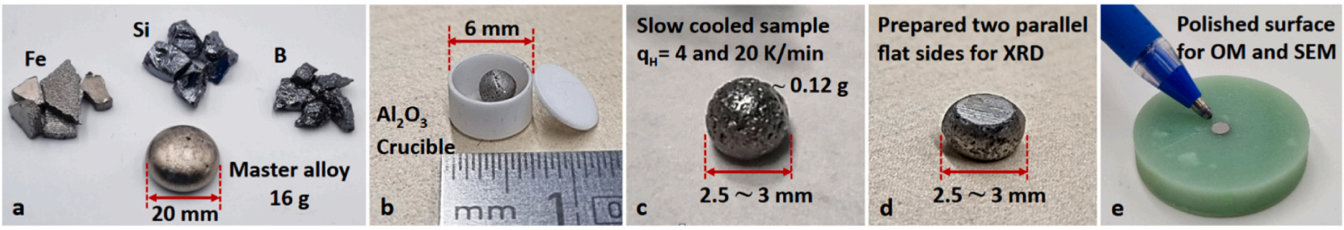

Fig. 1. The preparation of iron-silicon-boron samples: a) the homogenized ingot with a weight of about 16 g produced from the high-purity raw elements using an arc melter machine, b) the alumina (Al_2O_3) crucible for DTA experiments, c) the slow-cooled sample by DTA with the rates of 4 and 20 K/min and the average weight of 120 mg, forming a spherical shape, d) the prepared two parallel flat sides of the spherical sample through grinding for XRD measurements, e) the polished surface of the mounted sample for the microstructural study by OM and SEM.

Table 1
The list of investigated Fe-Si-B compositions and the thermal parameters at a heating rate (q_H) of 20 K/min.

Name Number	Composition (at%)	Temperature (q_H: 20 K/min)		Comment
		T_{eut} (±3 K)	T_l (±3 K)	
#1	$Fe_{80}\,Si_{10}\,B_{10}$	1394	1493	Ref. [29]
#2	$Fe_{78}\,Si_{13}\,B_9$	1390	1484	Ref. [2].
#3	$Fe_{75}\,Si_{10}\,B_{15}$	1386	1515	Ref. [30]
#4	$Fe_{74}\,Si_8\,B_{18}$	1389	1550	Ref. [18]
#5	$Fe_{78}\,Si_{11}\,B_{11}$	1382	1471	
#6	$Fe_{76}\,Si_{13}\,B_{11}$	1389	1471	
#7	$Fe_{76}\,Si_{15}\,B_9$	1387	1470	
#8	$Fe_{80}\,Si_{11}\,B_9$	1388	1511	
#9	$Fe_{80}\,Si_{13}\,B_7$	1388	1551	
#10	$Fe_{78}\,Si_{15}\,B_7$	1386	1516	
#11	$Fe_{74}\,Si_{15}\,B_{11}$	1388	1467	
#12	$Fe_{74}\,Si_{13}\,B_{13}$	1387	1489	
#13	$Fe_{76}\,Si_{11}\,B_{13}$	1382	1479	
#14	$Fe_{78}\,Si_9\,B_{13}$	1388	1473	
#15	$Fe_{80}\,Si_9\,B_{11}$	1389	1478	
#16	$Fe_{77}\,Si_{11}\,B_{12}$	1388	1464	Eutectic composition of this study

sides of the spherical sample to provide two parallel sides (Fig. 1d). The patterns were analyzed by PANalytical XPert HighScorePro software. The experiments were performed in Bragg-Brentano geometry, and the underlying principle is the Bragg law of diffraction, $n\lambda = 2d\sin\theta$ [31]. High-energy synchrotron X-ray diffraction (HEXRD) was performed on as-cast plate-shaped specimens in transmission geometry at room temperature at the P21.2 beamline of PETRA III Deutsches Elektronen-Synchrotron (DESY) in Hamburg. An X-ray energy of 70 keV ($\lambda = 0.17715$ Å) with a beam size of $500 \times 500\ \mu m^2$ was used. Diffraction patterns were collected using a VAREX XRD 4343CT area detector (2880×2880 pixels; $150 \times 150\ \mu m^2$ pixel size). The two-dimensional diffraction images were azimuthally integrated using PyFAI [32].

2.4. Microstructural study

Optical microscopy (OM) and scanning electron microscopy (SEM) utilizing a Zeiss NT Ltd. Sigma VP SEM at 20 kV acceleration voltage were used to examine the microstructures. Energy dispersive X-ray spectroscopy (EDS) and electron backscatter diffraction (EBSD) were used to map the local distribution of alloying elements and analyze the chemical compositions of the phases. The EBSD instrument was an Apreo 2S (ThermoFisher Scientific) FEGSEM, equipped with an Oxford Instruments EBSD detector. Measurements were conducted at a working distance of 13 mm, using an accelerating voltage of 20 kV, a beam current of 2.7 nA, and a step size of 100 nm.

The samples for OM and SEM examination were prepared using standard metallographic procedures by mounting the spherical samples in a resin, grinding with successively finer grades of silicon carbide (SiC) abrasive papers, and finally polishing using diamond suspensions with particle sizes of 3 μm and 1 μm, and 0.05 μm colloidal silica-based suspension, followed by thorough cleaning of the surface with ethanol and water (Fig. 1e).

3. Results and discussion

To find the eutectic point in the compositional space experimentally, DTA measurements were performed on four known alloys of $Fe_{80}Si_{10}B_{10}$ [29], $Fe_{78}Si_{13}B_9$ [2], $Fe_{75}Si_{10}B_{15}$ [30], and $Fe_{74}Si_8B_{18}$ [18], hereafter labeled as alloys #1, #2, #3, and #4, respectively. These compositionsselected from the literature, are indicated in the ternary Fe-Si-B triangle in Fig. 2a. The small gray triangle on the lower right side of Fig. 2a shows the explored area in this study and is magnified in Fig. 3 as the main investigation map.

The evaluation of the DTA results is based on the obtained melting peaks during the heating scans after the samples had been cooled slowly at 4 K/min. A eutectic alloy exhibits a sharp and distinct melting peak starting at an onset temperature corresponding to the eutectic temperature, T_{eut}, where all phases present in the eutectic microstructure melt simultaneously. For off-eutectic (non-eutectic) alloys, melting occurs over a broader temperature range, whereas the eutectic microstructure melts first and the remaining primary phase remelts later, appearing as a shoulder in the DTA signal. Therefore, in DTA scans, a sharp peak without a melting shoulder indicates that the alloy is close to the eutectic composition, while the existence of a shoulder on the melting peak shows partial melting, meaning an off-eutectic composition that contains a region where liquidus and solidus temperatures spread further apart and molten eutectic and still crystalline primary phase are present at the same time.

Fig. 2b shows four initial alloys DTA results, along with the derivatives of the DTA curves in the inset, highlighting all to be off-eutectic compositions as indicated by the pronounced shoulders. These shoulders are also identified by the second small minimum in the DTA curves derivatives. Alloys #3 and #4 are far from the eutectic because of their wide shoulders, while alloys #1 and #2 are closer to the eutectic composition due to their shorter shoulders. Between alloys #1 and #2, roughly similar thermal behavior, alloy #2 is chosen as the center point for the subsequent refinement since alloy #2 ($Fe_{78}Si_{13}B_9$) is the commercial alloy with the industrial name of Metglas 2605-SA1 [2]. In the first refinement step, the compositional zone of interest is drawn around alloy #2 with a circle of a two at% radius. This development results in alloys #5, #6, #7, #8, #9, and #10, which are represented by the open circles on the ternary triangle in Fig. 3.

The results of DTA measurements on the first set of developed alloys, shown in Fig. 4, reveal that alloys #8, #9, and #10 are off-eutectic due to the appearance of a pronounced shoulder, while alloys #5, #6, and #7 are closer to the eutectic point, suggesting the possibility of eutectic formation in their vicinity. Therefore, staying B-rich and moving towards the B-richer side, a second set of alloys was prepared as indicated in the ternary triangle of Fig. 3, numbered #11, #12, #13, #14, and #15, and represented by solid black circles. Table 1 lists the

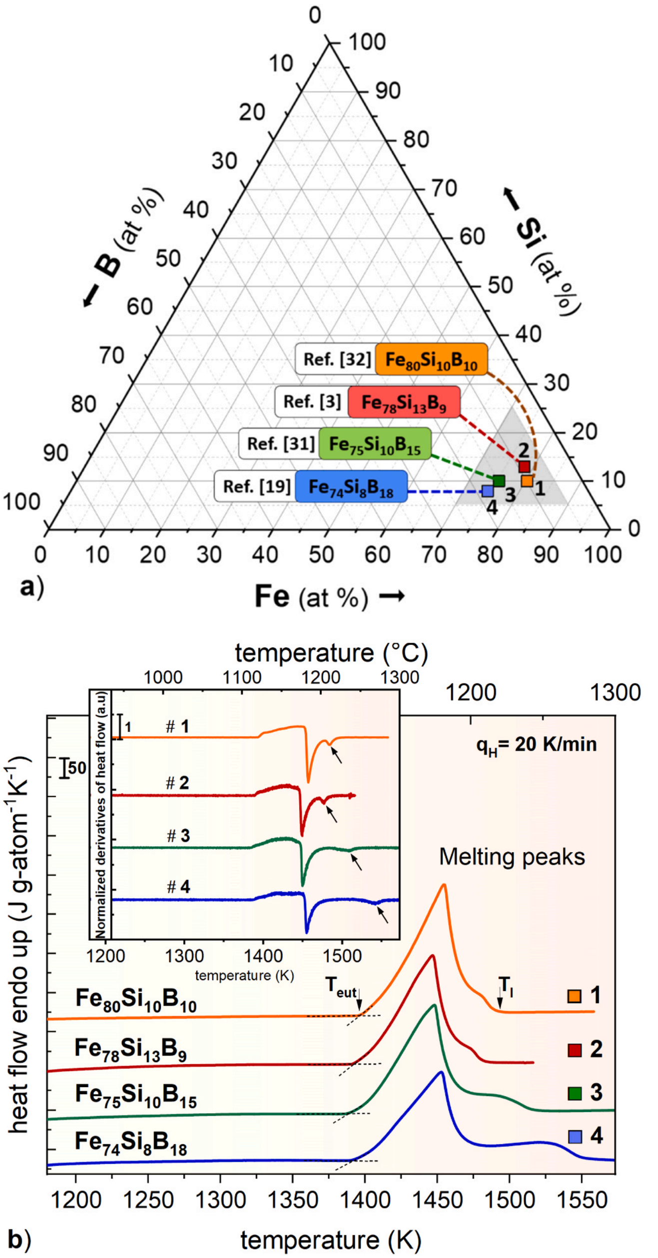

Fig. 2. Selected alloys #1, #2, #3, and #4 from literature as starting points to explore the eutectic composition. a) Position of the four compositions on the Fe-Si-B ternary phase diagram. The gray triangle represents the explored zone based on sixteen studied compositions. b) DTA scans of alloys #1 to #4. The inset shows the corresponding derivatives. All four alloys exhibit off-eutectic behavior as indicated by the presence of shoulders caused by the remelting of the primary phase.

compositions with the measured eutectic temperature, T_{eut}, and the liquidus temperature, T_l.

Among the DTA results of the second set of developed alloys, presented in Fig. 4, only alloy #15 shows a visible shoulder, indicating its off-eutectic behavior, while the absence of a shoulder in the melting curves of alloys #11, #12, #13, and #14 indicates that they are close to the eutectic point. Consequently, a more sensitive approach to determining the eutectic point involves analyzing the first derivative of the heat flow curve, which enables the detection of subtle changes in the melting curve pinpointing the eutectic composition more accurately. The derivative is obtained by calculating the slope of the tangent line to the curves, representing the rate of change in the heat flow at each temperature.

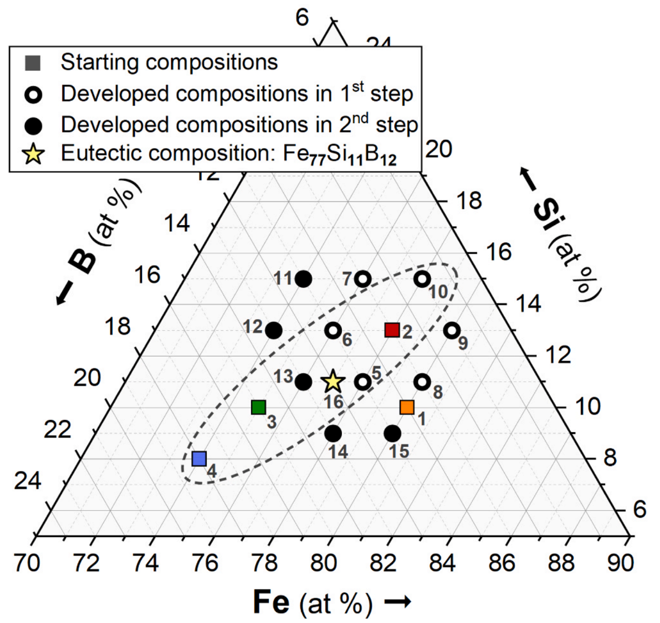

Fig. 3. Position of the investigated Fe-Si-B compositions in the ternary triangle. The squares are the starting compositions extracted from literature. The circles represent the developed compositions from the 1st and 2nd rounds of investigation, depicted by hollow and solid circles, respectively. The star symbol shows the eutectic point identified in this study. The elliptical region (dashed) shows the compositions considered in the XRD and microstructural analyses.

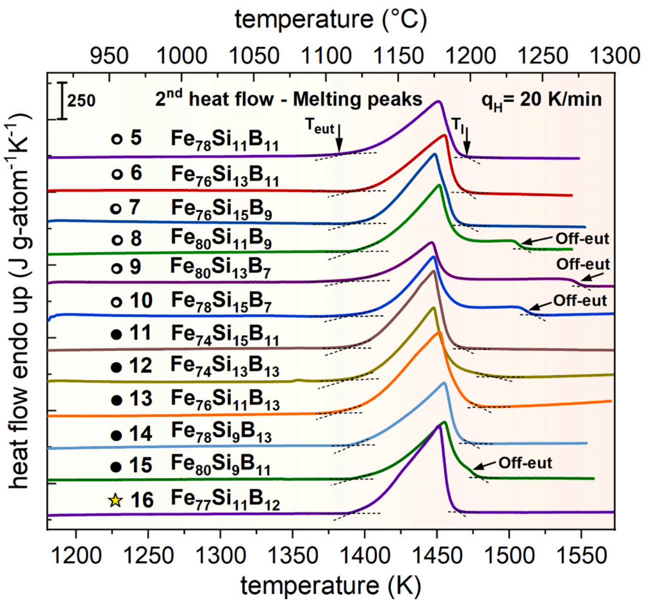

Fig. 4. DTA up scans for the melting events of the twelve developed alloys, arranged from alloys #5 to #16. The hollow circles and the solid circles represent the developed alloys in the 1st and 2nd investigation rounds, respectively. Melting peaks with a pronounced shoulder depict an off-eutectic behavior.

Fig. 5a shows the heat flow curves as well as the derivatives of the heat flow for a close-eutectic and a clearly off-eutectic composition. For the alloy that is close to the eutectic composition (alloy #6), the heat flow remains nearly constant in the crystalline state (below T_{eut}), resulting in a first derivative close to zero. At T_{eut}, the heat flow rapidly increases as the material absorbs heat, causing the first derivative to rise

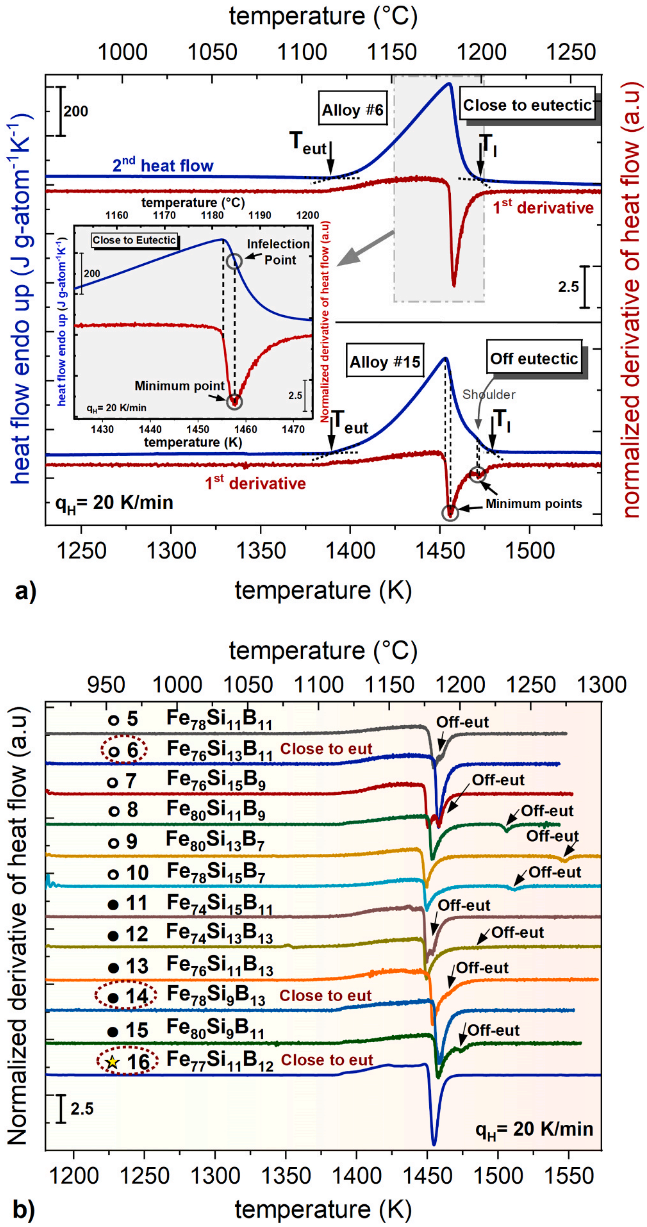

Fig. 5. Derivatives of the heat flows: a) The illustration of the DTA heat flows (blue scan) and the corresponding normalized derivatives (red scan) of the close to eutectic (#6) and off-eutectic (#15) compositions as a function of temperature. b) Normalized derivatives of the heat flow for alloys #5 to #16, showing alloys #6, #14, and #16 to be the closest to the eutectic due to the single and sharp dip (downward peak). The study of the microstructure identifies #16 as the final closest composition to the eutectic point.

with a gentle slope. This rise remains relatively constant, reflecting a steady rate of heat absorption until reach the peak of the melting event. Beyond the peak, the heat flow decreases, and the first derivative drops sharply, signaling the high rate of change in heat flow associated with the eutectic phase transition. The inflection point in the melting peak of the heat flow is represented as the minimum point in the derivative, as shown in the inset of Fig. 5a. The heat flow, past the inflection point, continues to decrease at a slower rate until it reaches the baseline again. At this stage, the derivative approaches zero, indicating that there are no further changes in the heat flow. This temperature is formally labeled T_l, as it signifies when the alloy has completely melted. For a true eutectic alloy, this temperature would approach T_{eut} as the heating rate of the DTA experiment is continuously decreased. The peak would become increasingly sharp, and T_l would merge with T_{eut} for a hypothetical quasi-static, infinitely slow heating experiment. For the off-eutectic alloy (#15), the shoulder of the melting peak leads to a second minimum in the derivative with its minimum corresponding to the inflection point of the shoulder, and here T_l roughly corresponds to the liquidus temperature of the off-eutectic alloy. In our experiments with a heating rate of 0.333 K/s (20 K/min), the melting event is rather broad, e.g., is approximately 80 K wide for alloy #6 in Fig. 5a. This means that if the alloy is slightly off-eutectic, the re-melting of a small amount of primary phase that has formed upon initially cooling the melt might be hidden in the single melting peak. This means thermal analysis alone is insufficient to pinpoint the eutectic composition. This is the case for alloy #6, which distinctly displays a minor proportion of primary dendrites, as seen in Fig. 8.

Fig. 5b shows the normalized derivatives of the DTA heat flows for the twelve new alloys. Based on their microstructures shown in Fig. 8, alloys #6 and #14 are determined to be closest to the eutectic point, as they exhibit no shoulders in the heat flow and no secondary dip in their derivatives. Consequently, alloy #16 was prepared between the two alloys, noting that adjacent compositions numbers 5 and 13 are slightly off-eutectic. The DTA heat flow of alloy #16 and its derivative are shown in Fig. 4 and Fig. 5b, respectively. The derivative of alloy #16 displays a single sharp dip, similar to that of alloys #6 and 14, indicating that these three are located in a eutectic trench. Therefore, microstructural analyses are employed to further clarify the eutectic point between alloys #6, #14, and #16 by detecting the primary phases and the fraction of eutectic microstructure (lamella formation).

The potential solidified phases of the studied alloys are predictable by the isothermal section of the Fe-Si-B ternary phase diagram at 1273 K (1000 °C), as shown in Fig. 6, which was calculated by the CALPHAD method [18]. According to the position of the studied compositions on the phase diagram for 1273 K (about 115 K below the eutectic temperature), most of the studied compositions are located within a large two-phase region, [(bcc + B2) + Fe_2B]. Therefore, according to the tie-lines, these alloys are anticipated to predominantly exhibit a mixture of body-centered tetragonal (BCT) iron boride (Fe_2B) and Fe-Si phases. The Fe-Si phases correspond to the body-centered cubic (BCC) α-Fe solid solution (labeled 'bcc' in Fig. 6, capable of dissolving Si) and potentially the ordered BCC-based iron silicide Fe_3Si (associated with the B2 phase field indicated on the diagram). Additionally, due to the proximity of

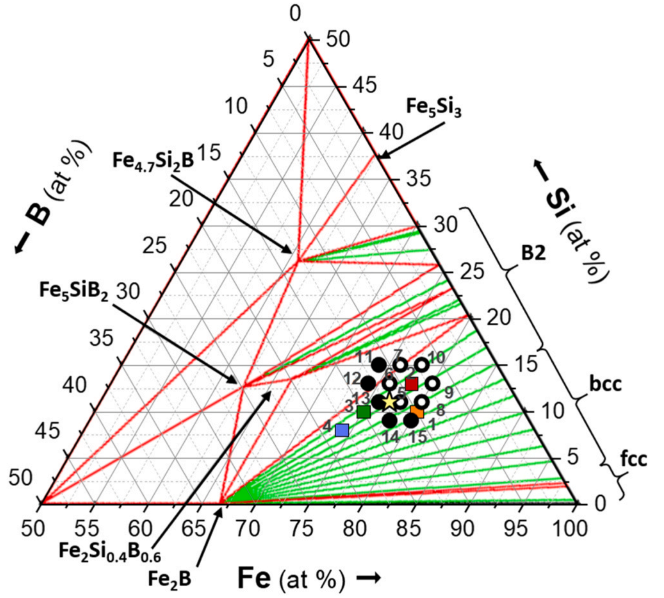

Fig. 6. The position of the sixteen investigated Fe-Si-B compositions on an isothermal section of the stable phase diagram at 1273 K (1000 °C) [18].

alloys #7, #11, and #12 to the relevant phase field boundary, a small amount of an additional phase, $Fe_2Si_{0.4}B_{0.6}$, could be present for these specific compositions. The XRD analyses presented in Fig. 7 were used to verify the presence of predicted phases in the studied alloys.

Fig. 7 illustrates the XRD results of eight selected alloys to show which crystalline phases formed upon solidification, spanning the compositional range from the Si-rich side (alloy #10) to the B-rich side (alloy #4). At the bottom of the figure are included the reference diffraction patterns of α-Fe, Fe_3Si, and Fe_2B phases expected based on the Fe-Si-B ternary system and the phase diagram of Fig. 6, which facilitates phase identification and peak indexing [33–35]. The XRD patterns confirm the presence of solidified phases, α-Fe, Fe_3Si, and Fe_2B in the investigated alloys. A prominent diffraction peak observed consistently across all measured compositions is located in the 2θ range of 44–46°. This strong reflection corresponds predominantly to the overlapping main peaks of α-Fe ([110]) and Fe_3Si ([220]), indicating the presence of the Fe-based matrix phase throughout the compositional series. The relative intensities of the diffraction peaks associated with the different phases exhibit systematic variations as the alloy composition varies, reflecting the differing phase proportions in each sample [36]. Specifically, as the composition shifts from Si-rich (#10) towards B-rich (#4), signifying an increasing boron content relative to silicon, distinct trends are observable. The intensity of reflections associated with the Fe_3Si phase, such as the peak identified in the source text as the [110] reflection located near 2θ= 65° (within the cluster also containing Fe(α) [200] and Fe_3Si [400] indices marked on the figure), demonstrates a discernible decrease. This trend is consistent with the reduced volume fraction of the Si-rich Fe_3Si phase as the overall silicon content decreases across the series. Conversely, the characteristic diffraction peaks belonging to the Fe_2B phase, indexed at 2θ positions approximately equal to 25° ([110]), 35° ([020]), 42.5° ([002]), 50° ([112]/[220]), and 57° ([022]/[130]), show a progressive increase in intensity moving from alloy #10 towards alloy #4, which directly correlates with the increasing boron concentration in the alloys. Notably, the XRD patterns for the B-richer alloys #13, #3, and #4 exhibit particularly pronounced Fe_2B reflections. This increased intensity indicates a substantial volume fraction of the Fe_2B phase in these alloys, corroborating microstructural observations (shown in Fig. 8), which reveal significant amounts of primarily solidified Fe_2B phase in these B-richer compositions. In contrast, the Fe_2B reflections in the Si-richer alloys (#10 and #2) are considerably weaker. This is attributed to their lower overall boron content, resulting in a smaller overall volume fraction of the Fe_2B phase. According to the accompanying microstructural analysis and phase diagram considerations, Fe_2B primarily forms as part of the eutectic microstructure and not as a primary solidification phase in these Si-rich compositions, where Fe_3Si is the dominant primary phase.

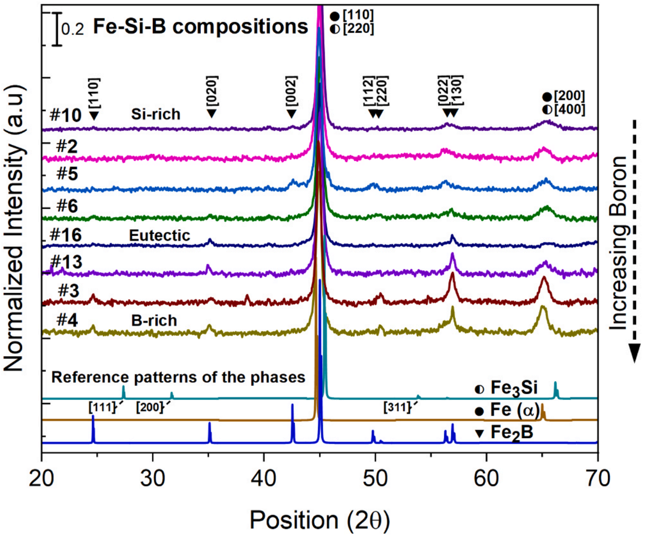

Fig. 7. X-ray diffractograms of the investigated Fe-Si-B slow-cooled samples span from the Si-rich side, alloy #10, toward the B-rich side, alloy #4. The reference patterns of the solidified phases are provided for comparison and indexing the reflections.

Fig. 8 presents a comprehensive overview of the evolving microstructures across selected Fe-Si-B alloys with varying compositions, solidified under controlled near-equilibrium conditions employing a slow cooling rate of 4 K/min. This figure systematically documents the evolution of solidification microstructures as a function of composition, shifting progressively from the Si-rich corner towards the B-rich side of the investigated Fe-Si-B alloys. The optical micrographs are arranged in the figure, with compositions indicated by alloy numbers (#) corresponding to the ternary diagram. The boron content is increasing from the top left to the bottom right.

Observing the alloys positioned in the Si-rich regime (first four micrographs), the microstructure is characteristically hypereutectic with respect to Si content relative to the ternary eutectic point. The dominant microstructural feature is the presence of a primary solidification phase exhibiting a distinct dendritic morphology [37,38]. As confirmed by subsequent EDS analysis (detailed in Fig. 9) and consistent with the equilibrium phase diagram, these dendrites correspond to the BCC α-Fe phase supersaturated with Si, commonly designated as the Fe(Si) solid solution [39]. Depending on the precise Si concentration and thermal history, this phase can exhibit atomic ordering, potentially forming the Fe_3Si intermetallic compound within the dendrites [39]. These primary dendrites, appearing as intricately branched tree-like structures, often display crystallographically preferred growth orientations, representing the first solid phase to nucleate and grow from the parent liquid upon cooling below the liquidus temperature. The complex branching pattern is a consequence of growth instabilities at the solid-liquid interface, driven by thermal and constitutional undercooling gradients inherent during solidification [37].

As dictated by the lever rule applied to the relevant two-phase [Liquid + α-Fe(Si)/Fe_3Si] or potentially a three-phase field on the liquidus projection of the phase diagram [39], the volume fraction occupied by these primary α-Fe(Si)/Fe_3Si dendrites progressively diminishes as the alloy composition shifts towards the eutectic point, i.e., moving compositionally from alloy #10 towards #16. This trend is visually apparent in micrographs across alloys #10 to #2, #6, #5, and #16, respectively. The interdendritic regions, representing the space surrounding these primary dendrites, are subsequently filled with the eutectic matrix. This eutectic matrix solidifies when the remaining liquid composition reaches the eutectic composition and undergoes the eutectic reaction. It typically displays a finer microstructural scale than the primary dendrites [40]. The presence of these primary dendrites, formed prior to the final eutectic solidification, are also directly correlated with thermal analysis data (DTA scans, see Figs. 4 and 5), where the Si-rich alloys characteristically exhibit a distinct shoulder on the melting peak or a broadened melting range occurring at temperatures above the main eutectic melting peak, corresponding precisely to the melting of these α-Fe(Si)/Fe_3Si dendrites upon reheating.

Alloy #16 ($Fe_{77}Si_{11}B_{12}$) exhibits a different microstructure from its Si-richer neighbors. It is predominantly, if not entirely, composed of a fine, intimately intergrown, and well-defined lamellar morphology. This morphology, characterized by thin alternating lamellae of the constituent phases (well-demonstrated in Figs. 9c, 9d, and 9e), is the hallmark of a eutectic reaction, where the liquid phase transforms simultaneously into two solid phases growing cooperatively. The near-complete absence (or significant suppression) of discernible primary phases, neither α-Fe (Si) dendrites nor faceted Fe_2B, strongly supports the identification of alloy #16 as representing, or being very close to, the ternary eutectic composition within this system under a 4 K/min cooling rate. This microstructural observation aligns well with thermal analysis data, Figs. 4 and 5b, which revealed a sharp, single endothermic melting peak for alloy #16 upon heating, indicative of the simultaneous melting

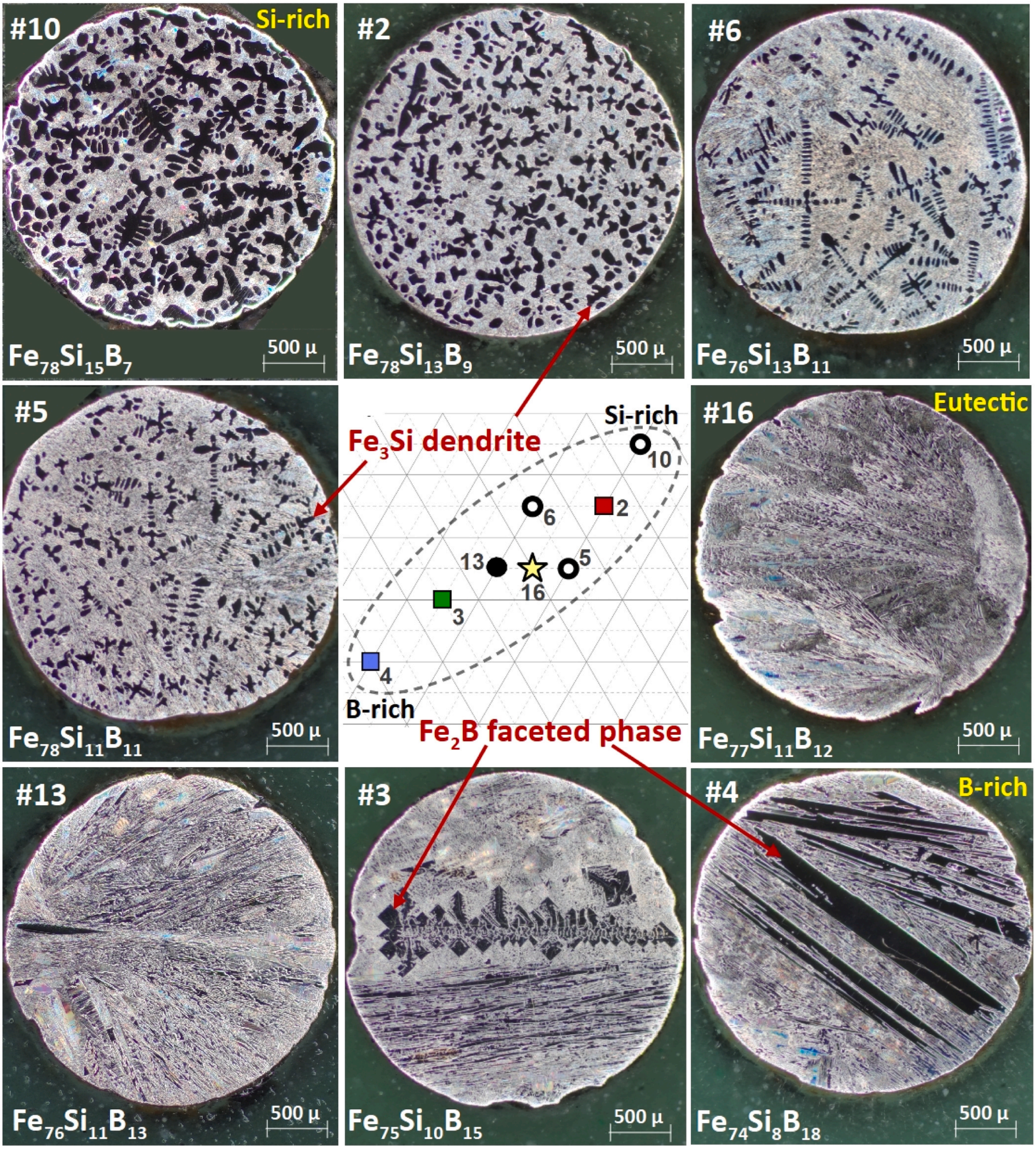

Fig. 8. Optical micrographs of Fe-Si-B alloys illustrating the evolution of solidification microstructures with a near-equilibrium cooling rate of 4 K/min. The figure demonstrates the transition from primary dendritic α-Fe(Si)/Fe_3Si solidification in Si-rich alloys (#10, #2), through eutectic structure near the ternary eutectic composition (#16), to primary faceted Fe_2B solidification in B-rich alloys (#3, #4). The inset ternary diagram indicates the alloy compositions (#). Scale bars: 500 µm.

characteristic of a well-defined eutectic point, with minimal or no post-melting signals (no-shoulder).

Finally, examining the alloys situated on the B-rich side of the eutectic composition (including alloys #13, #3, and #4), the primary phase changes. These compositions are hypereutectic with respect to boron. Here, the primary phase solidifying from the liquid is Fe_2B. Unlike the α-Fe(Si) phase, which exhibits non-faceted dendritic growth, Fe_2B possesses a distinct BCT crystal structure and exhibits anisotropic growth kinetics [41,42]. This leads to the formation of characteristically faceted primary crystals, clearly visible in the micrographs of alloys #3 and #4. These primary Fe_2B particles typically appear as blocky, angular, or somewhat rhombic shapes with flat interfaces and sharp

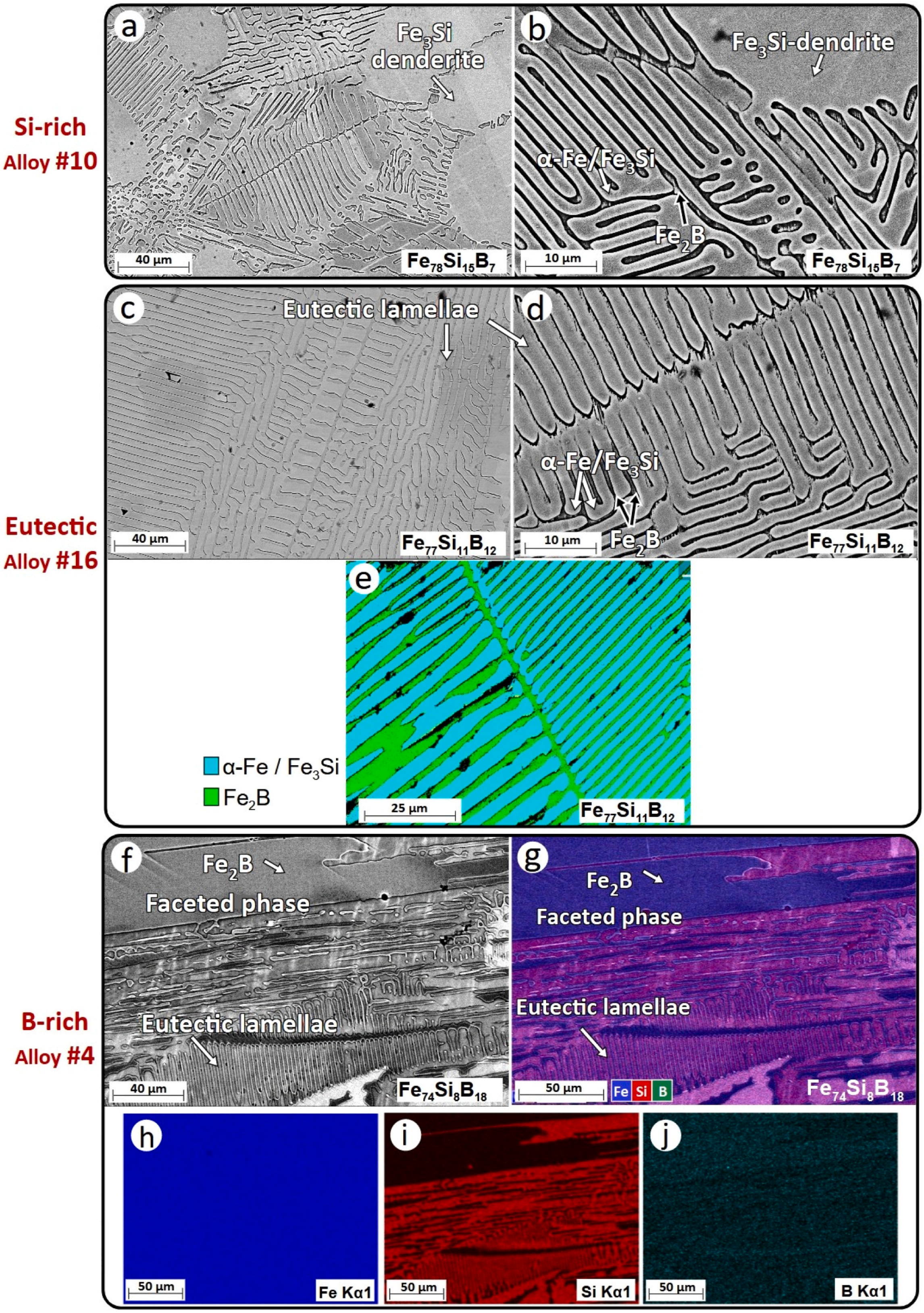

Fig. 9. Microstructure and phase identification in Fe-Si-B alloys at a 4 K/min cooling rate. (a, b) SEM/BSE images of the Si-richer alloy #10. (c, d) SEM/BSE images of the eutectic alloy #16, showing lamellar structure, confirmed by (e) EBSD phase map identifying α-Fe/Fe_3Si (light blue) and Fe_2B (green). (f) SEM/BSE image of B-richer alloy #4, showing primary faceted Fe_2B, confirmed by (g) composite EDS map and (h-j) individual Fe, Si, and B EDS maps.

corners. These faceted crystals nucleate and grow within the liquid phase once the temperature drops below the corresponding liquidus surface for these compositions. Subsequently, upon further cooling, the remaining liquid reaches the eutectic temperature and solidifies as the eutectic matrix, surrounding and embedding these primary Fe_2B crystals. Similar to the trend observed on the Si-rich side, but now driven by increasing boron content, the volume fraction and the average size of these primary faceted Fe_2B crystals become progressively larger as the composition moves further away from the eutectic composition towards the B-rich corner (compare #13, #3, and #4). This is particularly evident in alloy #4, where the large Fe_2B crystals dominate the microstructure. This observation is again a direct consequence of the lever rule applied within the two-phase region of the phase diagram (Liquid + Fe_2B) [43,44]. Correspondingly, the DTA scans for these B-richer alloys exhibit a distinct shoulder (Fig. 2) associated with the melting of the primary Fe_2B phase after the main eutectic melting peak upon reheating.

Fig. 9 illustrates a higher resolution characterization of microstructures and phase identification in Fe-Si-B alloys solidified at a cooling rate of 4 K/min, utilizing SEM, EBSD, and EDS. This figure provides detailed insights into the morphology and composition of the constituent phases for Fe-richer alloy #10 ($Fe_{78}Si_{15}B_7$) in images a-b, the eutectic alloy #16 ($Fe_{77}Si_{11}B_{12}$) in images c-d-e, and B-richer alloy #4 ($Fe_{74}Si_8B_{18}$) in images f-g-h-i-j, complementing the overview presented in Fig. 8. Images a, c, and f depict lower magnification views at 500x, whereas images b and d provide higher magnification details at 2000x.

In the Si-rich alloy #4, image a, at 500x magnification, clearly shows the primary Fe_3Si dendrites, previously identified in Fig. 8, embedded within a eutectic matrix. The composition of the dendrites is identified using EDS analysis and reveals nearly consistent composition of the Fe_3Si phase across multiple test points. We find $Fe_{79.1}Si_{20.9}$, with a standard deviation of ±3.3 at% for each component. Image b, at 2000x magnification, shows the finer details of the interdendritic region, confirming that it consists of a lamellar eutectic structure. This eutectic comprises alternating thick-bright lamellae and thin-dark lamellae. The thick-bright lamellae appear to branch directly and continuously from the dendrites, indicating they share the same phase composition Fe_3Si. Accurately determining the composition of individual thin lamellae with average thicknesses around 2.5–3 μm (similar in size to that measured in alloy #16) using conventional EDS is challenging due to the interaction volume of the electron beam exceeding the lamella width, leading to signal contribution from adjacent lamellae [45]. Furthermore, the detection of α-Fe and Fe_3Si using SEM/EDS presents certain challenges due to the overlapping X-ray emission lines in Fe and Si EDS spectra, which complicates precise quantification within the Fe-Si phases when distinguishing closely spaced elements [46]. Nonetheless, it is deduced that the thick-bright lamellae consist of α-Fe/Fe_3Si. Consequently, the thin-dark lamellae correspond to the Fe_2B phase. The EBSD analysis of the eutectic alloy (image e) also reveals the thin-dark lamellae as the Fe_2B phase.

Images c, d, and e illustrate the microstructure of the eutectic alloy #16. Image c, at 500x, showcases a remarkably homogeneous microstructure across the field of view, characterized by the absence of primary phases and consisting entirely of the eutectic microstructure. The eutectic exhibits colonies of lamellae oriented in various directions, typical of solidification initiated from multiple nucleation points. Image d, captured at a higher magnification of 2000x, provides a detailed view of the well-arranged lamellar morphology within a single colony. Measurements taken over a longitudinal interval revealed approximately 25 evenly spaced lamellae, yielding an average thickness of about 2.5 μm per lamella. This uniformity and well-defined spacing are characteristic of stable, coupled eutectic growth occurring under precisely controlled slow cooling conditions, ensuring a near-equilibrium solidification pathway. Image e presents an EBSD map from a region of alloy #16 eutectic structure. EBSD analysis, which identifies crystalline phases based on their crystallographic structure, clearly distinguishes the two constituent phases of the eutectic: the α-Fe/Fe_3Si phase (indexed and colored green) and the Fe_2B phase (indexed and colored light blue).

In the B-rich alloy #4, image f, at 500x magnification using the BSE detector, displays the primary faceted Fe_2B crystals embedded within the surrounding lamellar eutectic matrix. The Fe_2B crystals exhibit their characteristic blocky and angular morphology with sharp interfaces. Notably, the faceted Fe_2B phase appears significantly darker in the BSE image compared to the surrounding eutectic matrix. This contrast arises because the average atomic number of Fe_2B is lower than that of the Fe-Si-rich eutectic matrix, resulting in a smaller electro backscattered intensity being detected from the Fe_2B phase [47]. Image g shows a composite EDS map overlaid on the SEM image, visualizing the spatial distribution of the main elements: Fe (red), Si (blue), and B (green). Images h, i, and j present the individual EDS elemental maps for Fe, Si, and B, respectively. The EDS analysis shows the enrichment of boron within the faceted crystals, while silicon is predominantly located in the surrounding eutectic matrix, thus confirming the faceted phase as Fe_2B. Obtaining a reliable map for boron (image j) using EDS is inherently challenging due to its low atomic number, which results in low X-ray fluorescence yield and significant X-ray absorption effects. However, detection was made possible by optimizing analytical conditions, i.e., specifically reducing the accelerating voltage to below 20 kV, meaning minimizing excitation volume and matrix fluorescence, and coupling it with using a larger spot size or longer acquisition time (increasing signal counts) to improve the signal-to-noise ratio and enhance detection sensitivity for the light element boron [48,49].

The onset-to-endset temperature difference of the melting event ($\Delta T_m = T_l - T_{eut}$) is shown in Fig. 10 for the main studied alloys to assess their consistency with the eutectic melting behavior under identical experimental conditions. The eutectic (#16) and close-eutectic (#6) compositions exhibit a single sharp melting peak in all heating rates of 2, 4, 20, and 50 K/min (Fig. 10b and c). Their ΔT_m increases moderately with the heating rate from ~25 K at 2 K/min to ~75 K at 50 K/min, which is consistent with kinetic and instrumental broadening effects commonly reported for eutectic alloys [50]. In contrast, the B-rich (#4) and Si-rich non-eutectic compositions exhibit systematically larger ΔT_m values and pronounced peak asymmetry at the same heating rates, reflecting a multi-stage melting. Despite the similarity in ΔT_m values between alloys #6 and #16, considering the combined experimental uncertainties and a temperature tolerance of ±3 K, microstructural investigations support the identification of alloy #16 as the eutectic."

To investigate the GFA, the high-energy X-ray patterns (HE-XRD) of suction-cast Fe-Si-B plates are provided in Fig. 11 for four representative compositions (#4: B-rich, #6: near-eutectic, #10: Si-rich, and #16: eutectic) across three thicknesses of 140 μm, 250 μm, and 350 μm. The diffraction profiles reveal the phase constitution and crystallinity of each alloy as a function of both composition and section thickness. Across all thicknesses, alloy #10 consistently exhibits sharp and well-defined peaks, indicating a high degree of crystallinity and phase stability. In contrast, alloys #4, #6, and #16 compositions show broader or less intense peaks, suggesting either partial amorphization or the presence of multiple phases with lower crystallinity. No significant shift in peak positions is observed with varying thickness, indicating that the phase structure remains largely unaffected by the studied thickness range. However, minor variations in peak intensity may reflect differences in texture or preferred orientation due to the cooling rate gradients across the plate thickness.

Alloys #6 and #16, due to the proximity to the eutectic, and alloy #4, owing to its high B content, exhibit a better GFA than alloy #10. This indicates that although the eutectic composition is generally considered a favorable point for selecting alloys with high GFA, it is not necessarily the optimal composition. In other words, the highest GFA does not arise solely from proximity to the eutectic point. The presence of GFA enhancer alloying elements, such as boron, can improve it even when the alloy composition deviates from the exact eutectic point. Therefore, the improvement in GFA arises from a combination of compositional effects and not exclusively from eutectic positioning.

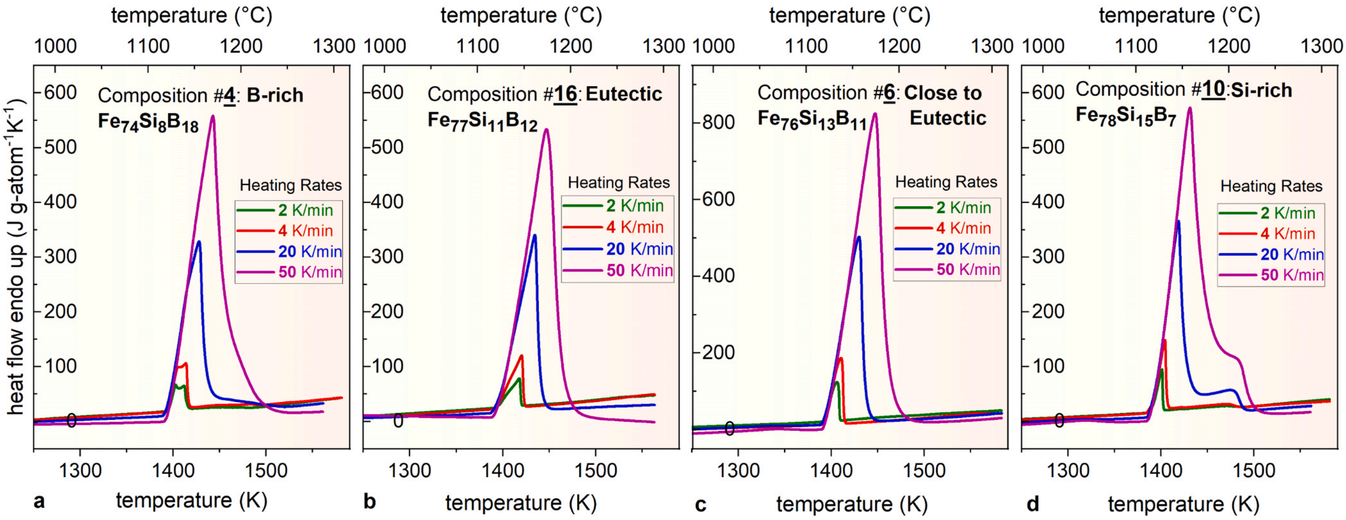

Fig. 10. DTA heating scans of key Fe-Si-B alloys measured at heating rates of 2, 4, 20, and 50 K/min: (a) B-rich composition #4, (b) eutectic composition #16, (c) near-eutectic composition #6, and (d) Si-rich composition #10. The eutectic alloy #16 exhibits a single sharp melting peak with a relatively narrow temperature interval ($\Delta T_m = T_l - T_{eut}$) of 20–30 K at low heating rates of 2 and 4 K/min, consistent with literature.

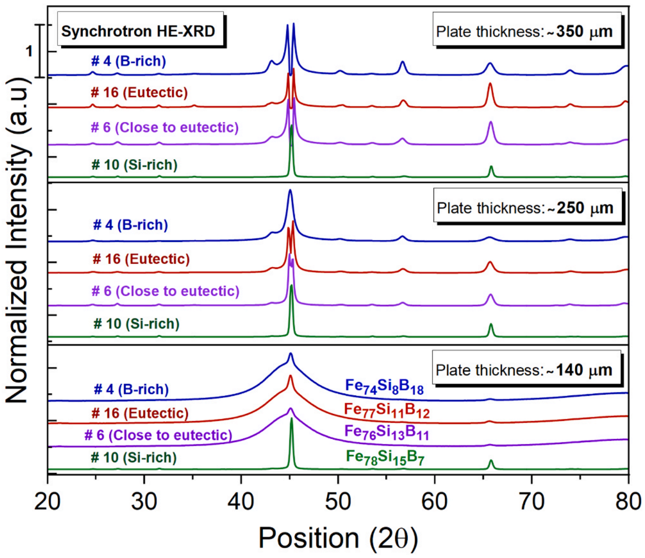

Fig. 11. High-energy X-ray diffraction patterns of suction-cast Fe-Si-B plates for four key compositions (#4, #6, #10, #16) at three thicknesses of 140 ± 10 µm, 250 ± 10 µm, and 350 ± 10 µm, highlighting phase evolution with composition and section thickness.

4. Summary and conclusion

This study resolves contradictions in the literature regarding the exact composition of the Fe-rich eutectic in the ternary Fe-Si-B alloy system through a systematic experimental investigation across a wide compositional range.

- The Fe-rich eutectic Fe-Si-B composition has been investigated and determined to be within a narrow eutectic valley centered approximately at $Fe_{77}Si_{11}B_{12}$ at%, using a synergistic methodology that combines sensitive thermal analysis (DTA scans and derivatives) with thorough microstructural and phase characterization (XRD, OM, SEM, EBSD, EDS).
- The corresponding eutectic temperature was determined to be 1388 K (1115 °C), with most solidus (eutectic) temperatures of the sixteen studied compositions measured within a narrow range of ± 2 K relative to this value.
- XRD analysis detected the equilibrium phases (α-Fe/Fe_3Si and Fe_2B) with systematic peak intensity variations reflecting the microstructurally observed phase fraction changes.
- Microstructural analysis by OM, SEM, EBSD, and EDS under near-equilibrium solidification (4 K/min) confirmed the eutectic nature of $Fe_{77}Si_{11}B_{12}$, revealing a well-defined lamellar structure of α-Fe/Fe_3Si and Fe_2B, devoid of primary phase formation, unlike adjacent off-eutectic compositions, exhibiting primary phases of Fe_3Si dendrites and Fe_2B faceted phases for Si-rich and B-rich compositions, respectively.
- The GFA of this system is dominated by both eutectic proximity and glass former elements, as B-rich ($Fe_{74}Si_8B_{18}$) and near-eutectic ($Fe_{76}Si_{13}B_{11}$) alloys exhibit superior GFA compared to Si-rich compositions and even outperform the exact eutectic alloy ($Fe_{77}Si_{11}B_{12}$). This confirms that maximum GFA does not necessarily occur at the exact eutectic point and may be enhanced by the glass former elements.

The accurate determination of the Fe-rich $Fe_{77}Si_{11}B_{12}$ eutectic has provided a validated starting point for subsequent alloy refinement strategies aimed at enhancing GFA and optimizing functional properties, e.g., magnetic behavior, through micro-alloying additions (e.g., Nb, Ni), exploiting the inherent glass-forming potential demonstrated across the investigated compositions. This is confirmed by XRD scans of the produced fully amorphous ribbons presented in the supplementary part (Fig. S1). The improvement of alloy properties, particularly in terms of GFA, by adding Nb and Ni is currently being investigated. However, this is beyond the scope of this work and will be reported in a separate publication. The further refinement and verification of the ternary eutectic invariant point would benefit from future studies employing diffusion couple experiments or CALPHAD-based thermodynamic calculations.

CRediT authorship contribution statement

Maria Teresa Perez-Prado: Investigation. **Isabella Gallino:** Writing – review & editing, Project administration, Funding acquisition. **Marcos Rodríguez-Sánchez:** Investigation. **Lucas Ruschel:** Writing – review & editing, Methodology. **Bastian Adam:** Writing – review & editing. **Amirhossein Ghavimi:** Writing – original draft, Validation,

Methodology, Investigation, Formal analysis, Conceptualization. **Maryam Rahimi Chegeni:** Writing – review & editing, Methodology, Investigation. **Ralf Busch:** Writing – review & editing, Supervision, Methodology, Funding acquisition.

Declaration of Competing Interest

The authors declare that they have no known competing financial interests or personal relationships that could have appeared to influence the work reported in this paper.

Acknowledgement

This work was carried out under the scope of the AM2SoftMag project, funded by the European Innovation Council through the HORIZON-EIC-2021-PATHFINDEROPEN-01 grant (GA No. 101046870). The authors thank the rest of the AM2SoftMag partners for their involvement in the project.

Appendix A. Supporting information

Supplementary data associated with this article can be found in the online version at doi:10.1016/j.mtcomm.2026.114741.

Data availability

Data will be made available on request.

References

[1] L. Yan, B. Yan, Y. Jian, Fabrication of Fe-Si-B based amorphous powder cores by spark plasma sintered and their magnetic properties, Materials 15 (2022), https://doi.org/10.3390/ma15041603.

[2] R. Kolano, K. Krykowski, A. Kolano-Burian, M. Polak, J. Szynowski, P. Zackiewicz, Amorphous soft magnetic materials for the stator of a novel high-speed PMBLDC motor, IEEE Trans. Magn. 49 (2013) 1367–1371, https://doi.org/10.1109/TMAG.2012.2234757.

[3] Y. Sun, X. Zhang, S. Wu, X. Zhuang, B. Yan, W. Zhu, C. Dolabdjian, G. Fang, Magnetomechanical properties of Fe-Si-B and Fe-Co-Si-B metallic glasses by various annealing temperatures for actuation applications, Sensors 23 (2023), https://doi.org/10.3390/s23010299.

[4] M.E. McHenry, M.A. Willard, D.E. Laughlin, Amorphous and nanocrystalline materials for applications as soft magnets, Prog. Mater. Sci. 44 (1999) 291–433, https://doi.org/10.1016/S0079-6425(99)00002-X.

[5] S. Pauly, L. Löber, R. Petters, M. Stoica, S. Scudino, U. Kühn, J. Eckert, Processing metallic glasses by selective laser melting, Mater. Today 16 (2013) 37–41, https://doi.org/10.1016/j.mattod.2013.01.018.

[6] X.P. Li, M.P. Roberts, S. O'Keeffe, T.B. Sercombe, Selective laser melting of Zr-based bulk metallic glasses: processing, microstructure and mechanical properties, Mater. Des. 112 (2016) 217–226, https://doi.org/10.1016/j.matdes.2016.09.071.

[7] M. Frey, J. Wegner, E.S. Barreto, L. Ruschel, N. Neuber, B. Adam, S.S. Riegler, H.-R. Jiang, G. Witt, N. Ellendt, V. Uhlenwinkel, S. Kleszczynski, R. Busch, Laser powder bed fusion of Cu-Ti-Zr-Ni bulk metallic glasses in the Vit101 alloy system, Addit. Manuf. 66 (2023) 103467, https://doi.org/10.1016/j.addma.2023.103467.

[8] M. Frey, J. Wegner, L.M. Ruschel, E.S. Barreto, S.S. Riegler, B. Adam, N. Ellendt, S. Kleszczynski, R. Busch, Additive manufacturing of Ni62Nb38 metallic glass via laser powder bed fusion, Prog. Addit. Manuf. (2025), https://doi.org/10.1007/s40964-025-01007-6.

[9] L. Thorsson, M. Unosson, M. Teresa Pérez-Prado, X. Jin, P. Tiberto, G. Barrera, B. Adam, N. Neuber, A. Ghavimi, M. Frey, R. Busch, I. Gallino, Selective laser melting of a Fe-Si-Cr-B-C-based complex-shaped amorphous soft-magnetic electric motor rotor with record dimensions, Mater. Des. 215 (2022) 110483, https://doi.org/10.1016/j.matdes.2022.110483.

[10] M. Rodríguez-Sánchez, S. Sadanand, A. Ghavimi, R. Busch, P. Tiberto, E. Ferrara, G. Barrera, L. Thorsson, H.J. Wachter, I. Gallino, M.T. Pérez-Prado, Relating laser powder bed fusion process parameters to (micro)structure and to soft magnetic behaviour in a Fe-based bulk metallic glass, Materialia 35 (2024) 102111, https://doi.org/10.1016/j.mtla.2024.102111.

[11] S. Sadanand, M. Rodríguez-Sánchez, A. Ghavimi, R. Busch, P. Sharangi, P. M. Tiberto, E. Ferrara, G. Barrera, L. Thorsson, H.J. Wachter, I. Gallino, M.T. Pérez-Prado, Laser powder bed fusion of a nanocrystalline Finemet Fe-based alloy for soft magnetic applications, J. Laser Appl. 36 (2024) 42029, https://doi.org/10.2351/7.0001391.

[12] D. Turnbull, G.S. Cargill, F. Spaepen, K.N. Tu, I. M.R.S.F.M.SPhase Transitions in Condensed Systems: Experiments and Theory: Festschrift in Honor of David Turnbull on the Occasion of His Seventieth Birthday: Symposium Held December 5-6, 1985, Boston, Massachusetts, U.S.A., Materials Research Society, 1987.

[13] D.B. Miracle, A structural model for metallic glasses, Nat. Mater. 3 (2004) 697–702, https://doi.org/10.1038/nmat1219.

[14] R. Busch, E. Bakke, W.L. Johnson, On the glass forming ability of bulk metallic glasses, Mater. Sci. Forum 235–238 (1997) 327–336, https://doi.org/10.4028/www.scientific.net/msf.235-238.327.

[15] R. Busch, The thermophysical properties of bulk metallic glass-forming liquids, JOM 52 (2000) 39–42, https://doi.org/10.1007/s11837-000-0160-7.

[16] R. Busch, J. Schroers, W.H. Wang, Thermodynamics and Kinetics of Bulk Metallic Glass, MRS Bull. 32 (2007) 620–623, https://doi.org/10.1557/mrs2007.122.

[17] I. Gallino, R. Busch, Physical Metallurgy of Bulk Metallic Glass-Forming Liquids. Thermodynamic and Kinetic Concepts in Glass Formation, Springer Nature, 2025.

[18] M.G. Poletti, L. Battezzati, Assessment of the ternary Fe–Si–B phase diagram, Calphad 43 (2013) 40–47, https://doi.org/10.1016/j.calphad.2013.08.001.

[19] A.I. Zaitsev, N.E. Zaitseva, A.A. Kodentsov, A thermodynamic study of liquid Fe-Si-B alloys; an influence of ternary associates on a liquid → glass transition, Metall. Mater. Trans. B 34 (2003) 887–898, https://doi.org/10.1007/s11663-003-0095-9.

[20] J. Jiao, B. Grorud, C. Sindland, J. Safarian, K. Tang, K. Sellevoll, M. Tangstad, The use of eutectic Fe-Si-B alloy as a phase change material in thermal energy storage systems, Materials 12 (2019), https://doi.org/10.3390/ma12142312.

[21] F.W.C.S. Smith, Constitution of iron-silicon-boron alloys, Trans. Am. Soc. Steel Treat. 18 (1930) 1023–1049.

[22] E. L, I. Lähteenmäki, The energy dispersive X-ray diffraction method: annotated bibliography 1968–78, J. Mater. Sci. 15 (1980) 269–278.

[23] V.G.V. Stuart Leslie Ames, Stephen David WashkoAmorphous Metal Alloy Strip and Method of Making Such Strip1986.

[24] M.A. Gibson, G.W. Delamore, Crystallization of stable and metastable eutectics in FeSiB metallic glasses, J. Mater. Sci. 25 (1990) 93–97, https://doi.org/10.1007/BF00544190.

[25] T. Yamasaki, T. Shimada, Y. Ogino, Composition dependence of viscosity of Fe-B-Si liquid alloy, J. Jpn. Inst. Met. 56 (1992) 1229–1234, https://doi.org/10.2320/jinstmet1952.56.11_1229.

[26] H. Huang, C. Yang, Q. Song, K. Ye, F. Liu, Nano-eutectic structure formation and soft magnetic properties of bulk ternary Fe-B-M (M = Si, Cu) alloys, J. Appl. Phys. 120 (2016) 43905, https://doi.org/10.1063/1.4959801.

[27] Y. Fan, A.M. Liu, Z. Chen, P.Z. Li, C.H. Zhang, Dynamic analysis of recalescence process and interface growth of eutectic Fe82B17Si1 alloy, J. Mater. Eng. Perform. 27 (2018) 1784–1791, https://doi.org/10.1007/s11665-018-3269-y.

[28] S. Yue, H. Zhang, R. Cheng, A. Wang, Y. Dong, A. He, H. Ni, C.-T. Liu, Magnetic and thermal stabilities of FeSiB eutectic amorphous alloys: compositional effects, J. Alloy. Compd. 776 (2019) 833–838, https://doi.org/10.1016/j.jallcom.2018.10.331.

[29] T. Tokunaga, H. Ohtani, M. Hasebe, Thermodynamic evaluation of the phase equilibria and glass-forming ability of the Fe–Si–B system, Calphad 28 (2004) 354–362, https://doi.org/10.1016/j.calphad.2004.11.004.

[30] A. Inoue, B. Shen, T. Ohsuna, Soft magnetic properties of nanocystalline Fe-Si-B-Nb-Cu rod alloys obtained by crystallization of cast amorphous phase, Mater. Trans. 43 (2002) 2337–2341, https://doi.org/10.2320/matertrans.43.2337.

[31] J.A. Hawreliak, S.J. Turneaure, Probing the lattice structure of dynamically compressed and released single crystal iron through the alpha to epsilon phase transition, J. Appl. Phys. 129 (2021) 135901, https://doi.org/10.1063/5.0042605.

[32] G. Ashiotis, A. Deschildre, Z. Nawaz, J.P. Wright, D. Karkoulis, F.E. Picca, J. Kieffer, The fast azimuthal integration Python library: PyFAI, J. Appl. Crystallogr. 48 (2015) 510–519, https://doi.org/10.1107/S1600576715004306.

[33] T.M. Project, Mater. Data Fe2B Mater. Proj. (2020), https://doi.org/10.17188/1274675.

[34] T.M. Project, Mater. Data Fe3Si Mater. Proj. (2020), https://doi.org/10.17188/1197276.

[35] T.M. Project, Mater. Data Fe Mater. Proj. (2020), https://doi.org/10.17188/1189317.

[36] Y. Li, L. Zhao, L. Lin, E. Li, Q. Cao, C. Wei, Relationships between X-ray diffraction peaks, molecular components, and heat properties of C-Type starches from different sweet potato varieties, Molecules 27 (2022), https://doi.org/10.3390/molecules27113385.

[37] P.C. Bollada, P.K. Jimack, A.M. Mullis, Faceted and dendritic morphology change in alloy solidification, Comput. Mater. Sci. 144 (2018) 76–84, https://doi.org/10.1016/j.commatsci.2017.12.007.

[38] Y. Ruan, A. Mohajerani, M. Dao, Microstructural and mechanical-property manipulation through rapid dendrite growth and undercooling in an Fe-based multinary alloy, Sci. Rep. 6 (2016) 31684, https://doi.org/10.1038/srep31684.

[39] K. Han, M. Saito, J. Xia, I. Ohnuma, R. Kainuma, Experimental determination of phase diagram involving silicides in the Fe-Si binary system, J. Alloy. Compd. 919 (2022) 165810, https://doi.org/10.1016/j.jallcom.2022.165810.

[40] L. Luo, Y. Tang, X. Liang, Y. Su, Y. Zhang, H. Xie, Optimizing the morphology and solidification behavior of Fe-rich phases in eutectic Al-Si-based alloys with different Fe contents by adding Mn elements, Materials 17 (2024), https://doi.org/10.3390/ma17164104.

[41] X.-Y. Song, Y.-J. Wang, J.-X. Zhang, D.-A. Du, J.-G. Xu, F. Peng, T.-T. Li, L.-J. Zhang, S.-L. Shu, X. Li, F. Qiu, Solidification microstructure manipulation mechanism of hypoeutectic and hypereutectic Al–Si alloys controlled by trace in-situ nano-Fe2B and nano-Fe3Si, J. Mater. Res. Technol. 21 (2022) 3856–3869, https://doi.org/10.1016/j.jmrt.2022.10.142.

[42] Y. Shao, J. Wang, Y. Liu, X. Miao, D. Fu, S. Cheng, P. Guo, Y. Zhang, F. Xu, Manipulation of the microstructure and properties of La(Fe,Si)13 alloys via solidification kinetics, J. Alloy. Compd. 944 (2023) 169147, https://doi.org/10.1016/j.jallcom.2023.169147.

[43] Y. Cai, D. Song, Y. Zhao, D. Yang, D. Zhang, W. Zhang, Effects of Fe content on the 3D morphology of Fe-rich phases and mechanical properties of cast Al-Mg-Si alloy, J. Alloy. Compd. 990 (2024) 174501, https://doi.org/10.1016/j.jallcom.2024.174501.

[44] M.C.J. Marker, B. Skolyszewska-Kühberger, H.S. Effenberger, C. Schmetterer, K. W. Richter, Phase equilibria and structural investigations in the system Al–Fe–Si, Intermetallics 19 (2011) 1919–1929, https://doi.org/10.1016/j.intermet.2011.05.003.

[45] M. Falke, I. Nemeth, Composition analysis by EDS at elevated temperatures and more, Microsc. Microanal. 25 (2019) 1430–1431, https://doi.org/10.1017/S1431927619007888.

[46] D. Newbury, N. Ritchie, M. Mengason, K. Scott, SEM/EDS trace analysis: limits imposed by fluorescence of the detector, St. Louis, MO, 2017, Microsc. Microanal. (2017), https://doi.org/10.1017/S1431927617005797.

[47] M. Čalkovský, E. Müller, D. Gerthsen, Quantitative analysis of backscattered-electron contrast in scanning electron microscopy, J. Microsc. 289 (2023) 32–47, https://doi.org/10.1111/jmi.13148.

[48] Y. Tsuchikawa, T. Kai, Y. Abe, K. Oikawa, J.D. Parker, T. Shinohara, I. Sato, Development of an areal density imaging for boron and other elements, J. Phys. Conf. Ser. 2605 (2023), https://doi.org/10.1088/1742-6596/2605/1/012022.

[49] E. Pitthan, M.V. Moro, S.A. Corrêa, D. Primetzhofer, Assessing boron quantification and depth profiling of different boride materials using ion beams, Surf. Coat. Technol. 417 (2021) 127188, https://doi.org/10.1016/j.surfcoat.2021.127188.

[50] I. Chang, Q. Cai, From simple binary to complex multicomponent eutectic alloys, Prog. Mater. Sci. 123 (2022) 100779, https://doi.org/10.1016/j.pmatsci.2021.100779.